Introduction

The supplementary contains 4 sections with 16 figures and 6 tables. In section S1, we demonstrated that the tropospheric delays were successfully corrected using the ERA5 weather model. In section 2, we listed the detailed information about the estimated model parameters for the three afterslip models. In section 3, we listed the detailed information about the estimated model parameters for the four aftershock models. And in section 4, we discussed whether viscoelastic relaxation mechanism can explain the early post-seismic deformation.

S1. Validation of the tropospheric delay correction

The stratified tropospheric delay is not random in time but seasonal, and varies with surface elevation, which means its spatial pattern always mimics elevation [47]. If there is a significant elevation difference between two locations, the stratified tropospheric delay varies with the seasons. Therefore, the InSAR LOS time series (after correcting the topography error) between these two locations can be dominated by the seasonal variations of tropospheric delay [48,49]. In this section, we investigate whether this phenomenon is reflected in our InSAR data and explore whether the ERA5 model describes the tropospheric delay well.

To investigate whether the ERA5 weather model properly described tropospheric delays related to this elevation difference, we considered the difference between a pixel located at the mountain foot and a reference pixel located at the Tianshan mountain (elevation difference of 2371 m over a horizontal distance of about 26 km; blue squares in Figure S1a). The InSAR range change (after correcting the topographic residuals) and the relative tropospheric delay time series calculated using ERA5 data (Figure S1c) have the same temporal trends, which indicates that the ERA5 weather model describes the tropospheric delay well in this area.

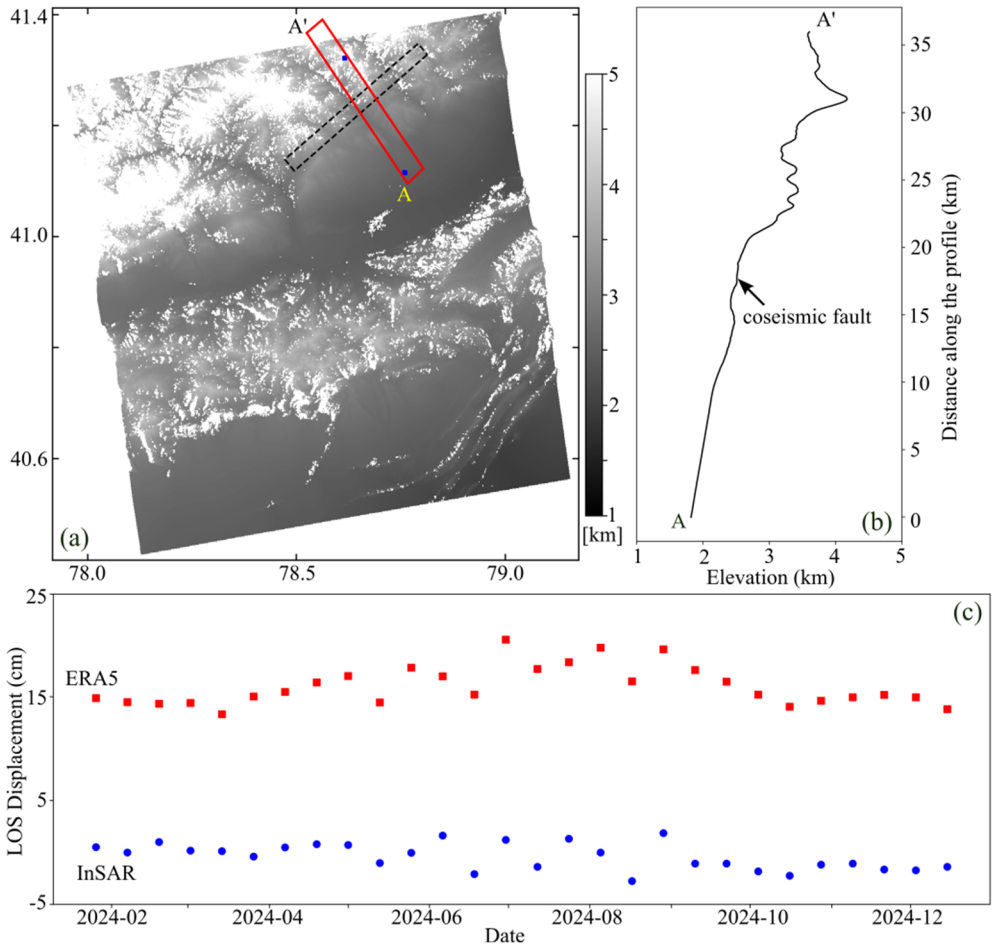

Figure S1. (a)-(b)Topography profiles perpendicular to the mainshock fault. Black dashed rectangle: coseismic fault of Yu's work. Red solid rectangle: profile. Blue points: two points used for (c). (c) InSAR LOS range change time series (blue points, after correcting topography error) between two points and the relative time series of tropospheric delay from ERA5 (red points) between the two points (locations at [41.32N, 78.62E] and [41.11N, 78.76E], elevation difference of 2371 m). A constant offset was added to ERA5 change data to separate the data.

S2. Model results for afterslip

S2.1 One-fault model

Table S1. Fault parameters for the afterslip from February 2024 to December 2024.

	Length (km)	Width (km)	Depth (km)	Dip (°)	Strike (°)	Rake (°)	Slip (m)	Lat* (°)	Lon* (°)	Mw	RMSE (cm)
					Segment1						
Min	1	1	0	0	180	0	0			6.05	0.88
Max	15	15	5	90	270	180	1	41.254	78.811		
Optimum	31.14	7.26	3.31	48.7	233.6	65.3	0.18				

94% HDI	24.25-38.42	5.00-9.55	2.67-3.89	40.9-55.9	231.4-235.7	56.1-75.1	0.13-0.22

*lat/lon: start point coordinate of the fault upper edge

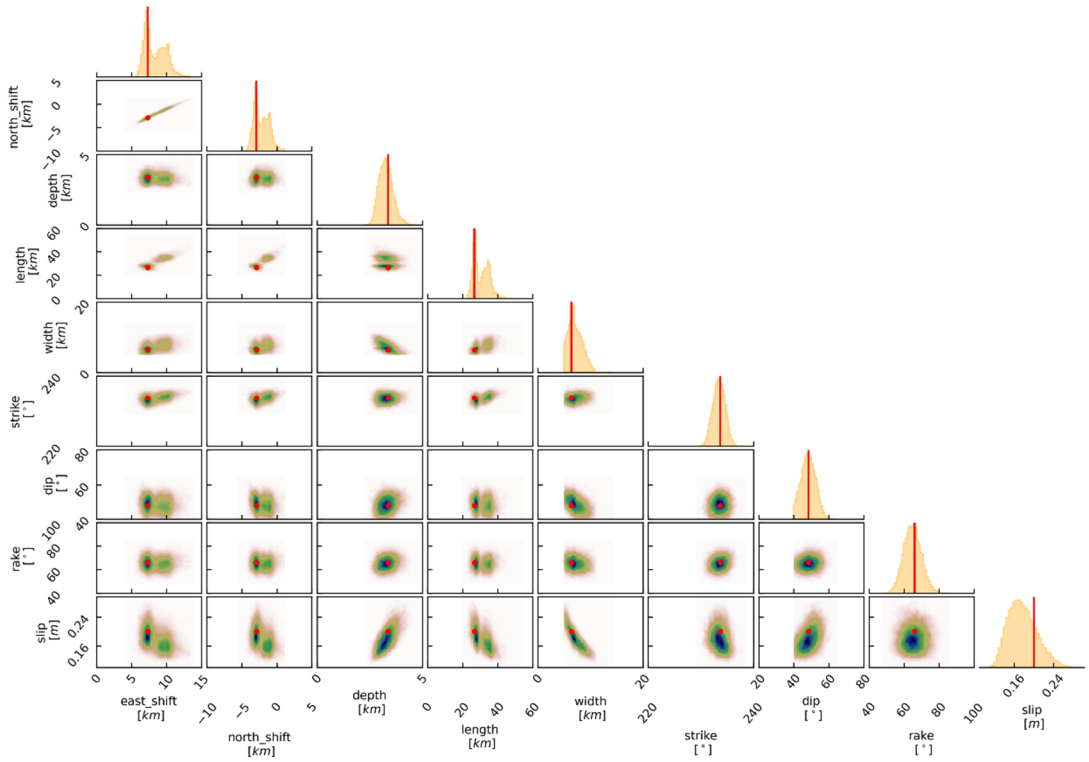

Figure S2. 1D/2D marginal posterior probability densities of the estimated fault parameters.

S2.2 Two-fault model

Table S2. Fault parameters for the afterslip from February 2024 to December 2024.

	Length (km)	Width (km)	Depth (km)	Dip (°)	Strike (°)	Rake (°)	Slip (m)	Lat* (°)	Lon* (°)	Mw	RMSE (cm)
					Segment1						
Min	1	1	0	0	180	0	0				
Max	15	15	5	90	270	180	1				
Optimum	8.57	6.57	3.09	50.3	231.3	70.3	0.31	41.162	78.65		
94% HDI	6.79-10.82	3.06-9.97	2.37-3.91	42.9-57.9	224.7-238.3	58.5-83.2	0.19-0.46			6.00	0.72
					Segment2						
Min	1	1	0	0	180	0	0				
Max	15	15	5	90	270	180	1	41.191	78.754		
Optimum	9.17	7.72	2.49	54.7	258.3	68.8	0.23				

94% HDI	4.20-12.43	3.61-11.48	1.73-3.34	47.2-60.0	250.7-268.5	55.3-82.6	0.12-0.39

*lat/lon: start point coordinate of the fault upper edge

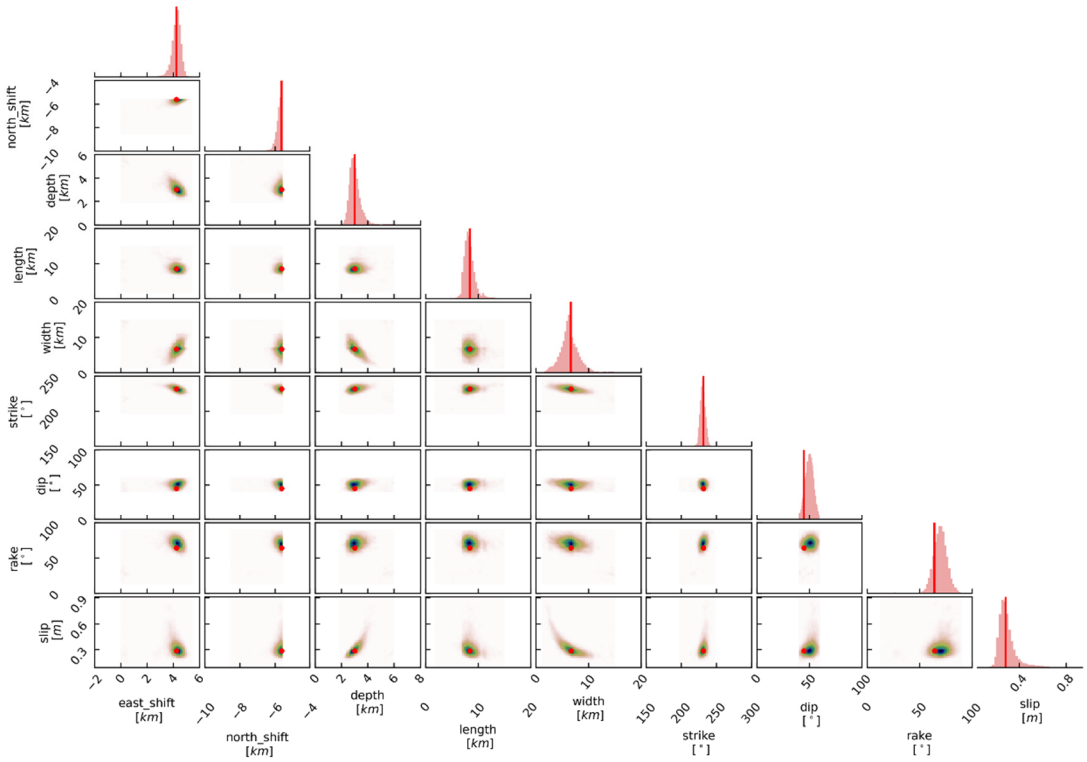

Figure S3. 1D/2D marginal posterior probability densities of the estimated fault parameters for segment 1.

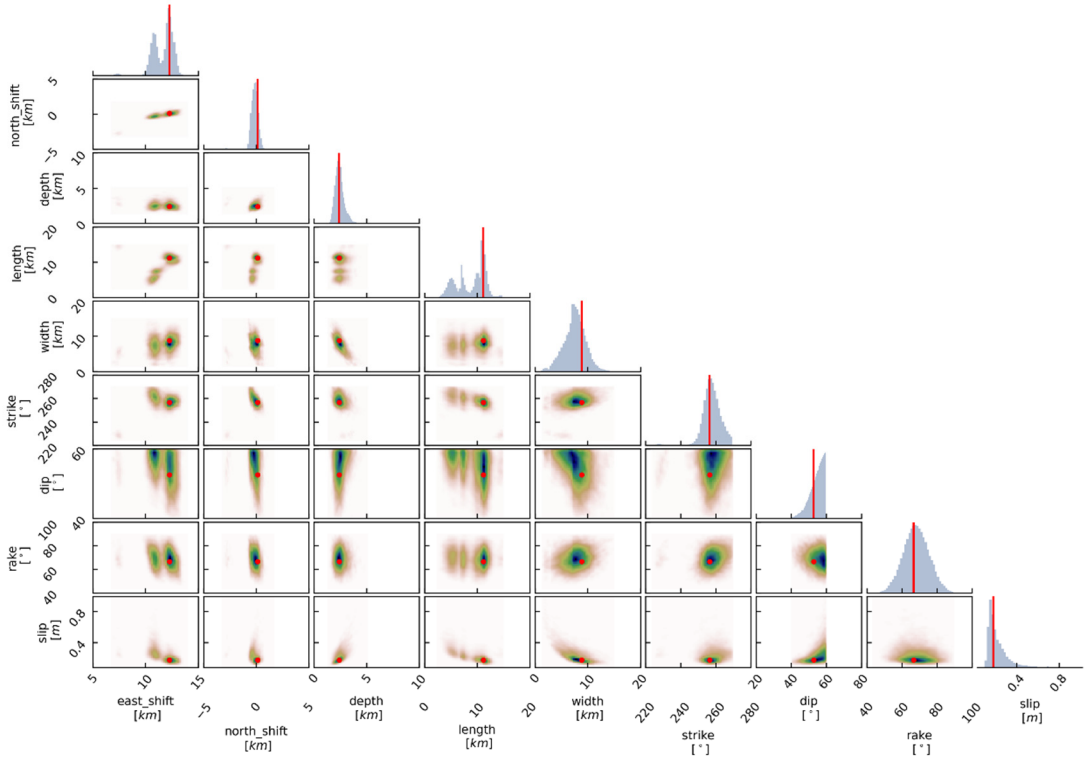

Figure S4. 1D/2D marginal posterior probability densities of the estimated fault parameters for segment 2.

S2.3. Three-fault model

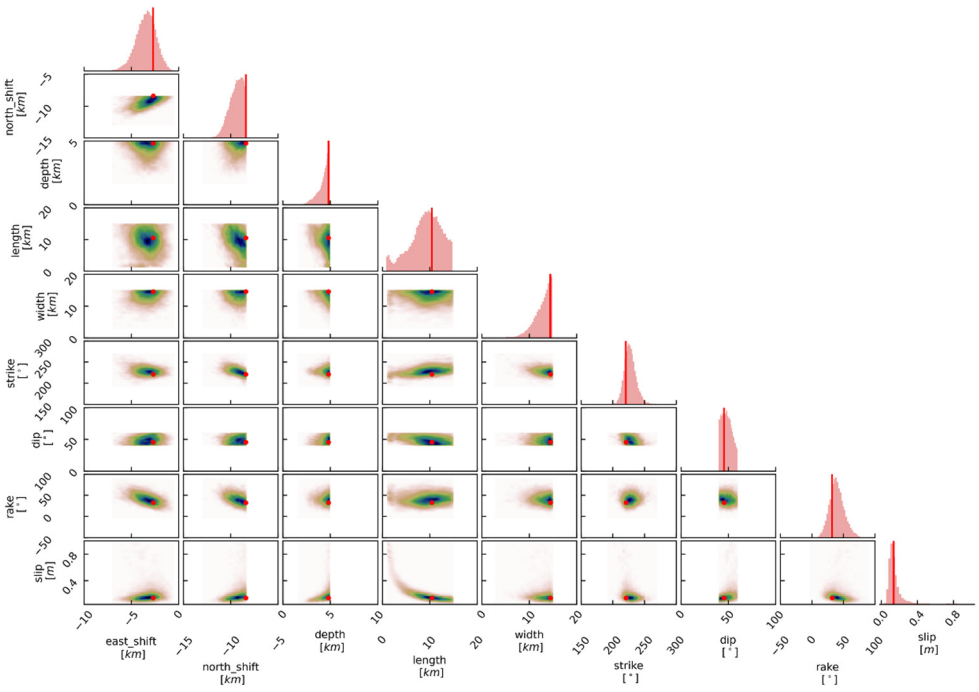

Figure S5. 1D/2D marginal posterior probability densities of the estimated fault parameters for the south segment.

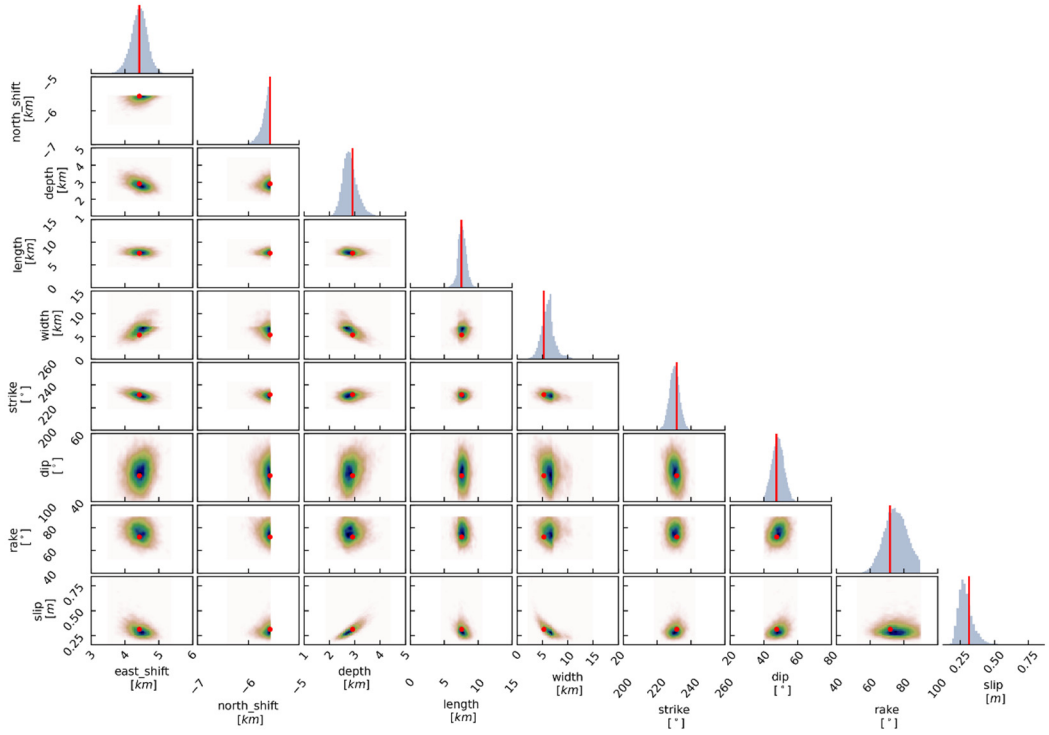

Figure S6. 1D/2D marginal posterior probability densities of the estimated fault parameters for the middle segment.

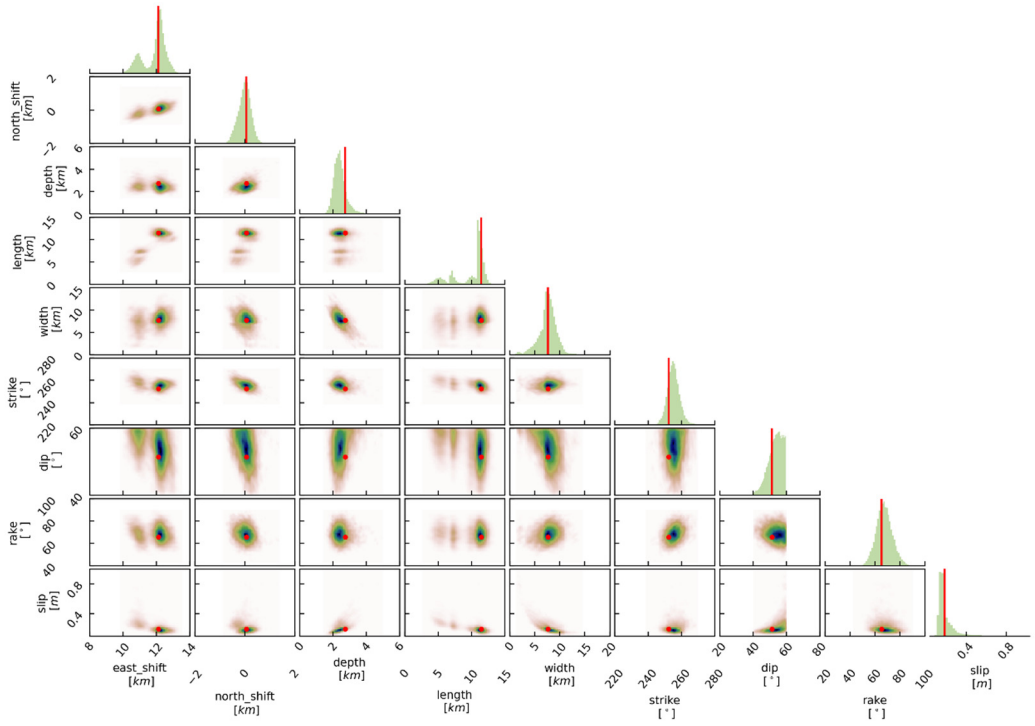

Figure S7. 1D/2D marginal posterior probability densities of the estimated fault parameters for north segment.

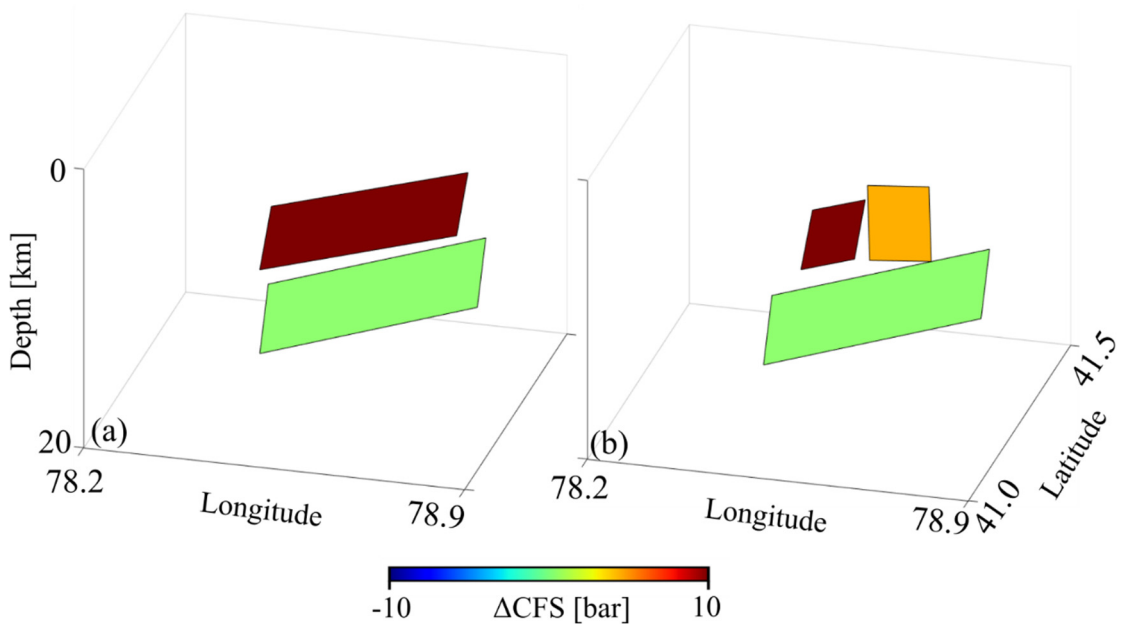

Figure S8. Coulomb stress changes in the direction of inferred slip along the afterslip fault segments imparted by the coseismic slip distribution. The green rectangle is the coseismic fault and the green color doesn't indicate any stress change. (a) is for the one-fault model and (b) is for the second fault model

S3. Aftershock occurred on 29 January

S3.1 SW-dipping one-fault model

Table S3. Seismogenic fault parameters for the SW-dipping one-fault model.

	Length (km)	Width (km)	Depth (km)	Dip (°)	Strike (°)	Rake (°)	Slip (m)	Lat* (°)	Lon* (°)	Mw	RMSE (cm)
Min	-*	-	0	-	-	80	0				
Max	-	-	5	-	-	100	5				
Optimum	9	5	1.3	41	70	90	0.43	41.14	78.57	5.81	4.82
94% HDI	-	-	1.16-1.48	-	-	-	0.40-0.46				

-*: fixed parameters

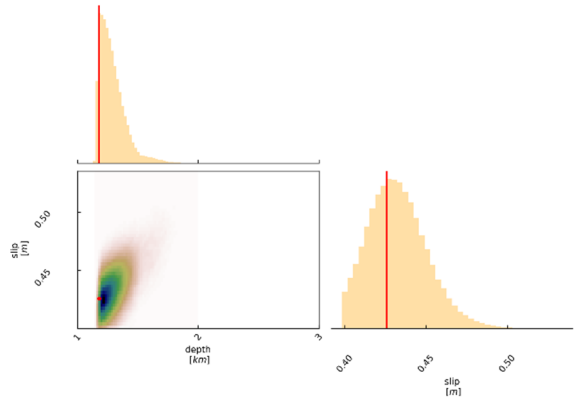

Figure S9. 1D/2D marginal posterior probability densities of the estimated fault parameters.

S3.2 NE-dipping one-fault model

Table S4. Seismogenic fault parameters for the NE-dipping one-fault model.

	Length (km)	Width (km)	Depth (km)	Dip (°)	Strike (°)	Rake (°)	Slip (m)	Lat* (°)	Lon* (°)	Mw	RMSE (cm)
Min	0	0	0	0	0	0	0				
Max	30	20	10	90	270	180	8				
Optimum	4.09	5.53	2.19	61.36	240.83	116.08	1.16				
94% HDI	3.15-4.99	4.18-6.99	1.79-2.60	59.31-63.37	238.40-243.25	108.71-123.19	0.79-1.55	41.14	78.63	5.60	4.91

*lat/lon: start point coordinate of the fault upper edge

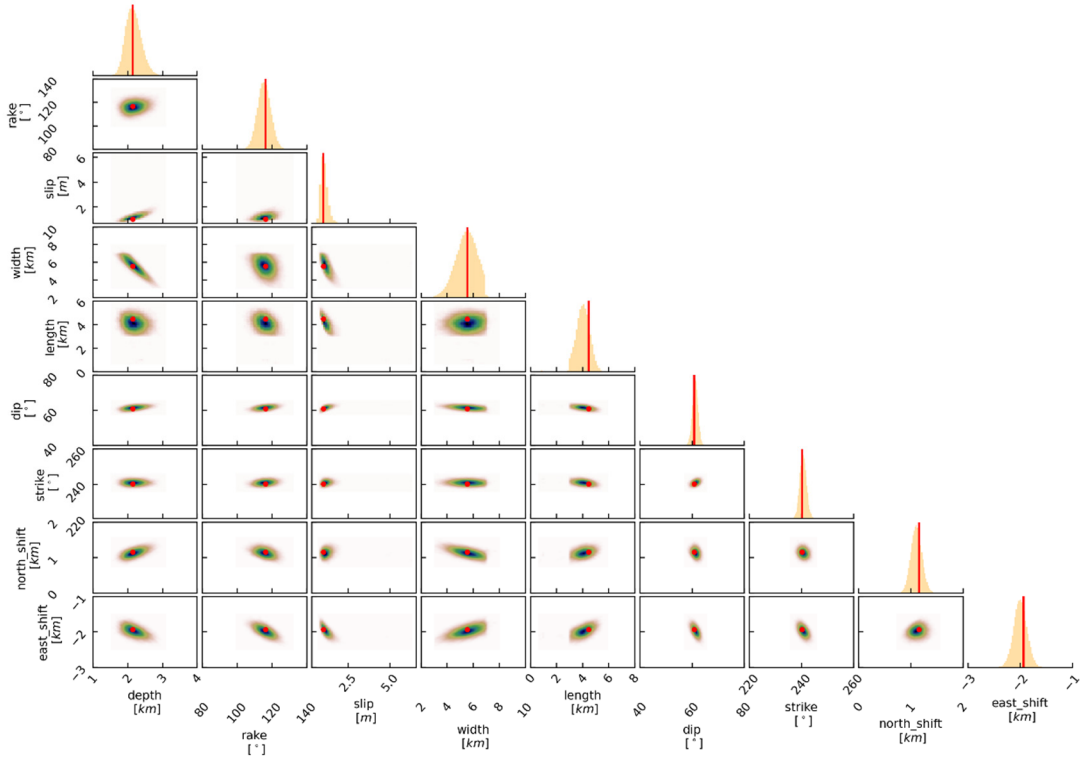

Figure S10. 1D/2D marginal posterior probability densities of the estimated fault parameters.

S3.3 NE-dipping two-fault model

Table S5. Seismogenic fault parameters for the aftershocks the occurred on 29 January 2024.

	Length (km)	Width (km)	Depth (km)	Dip (°)	Strike (°)	Rake (°)	Slip (m)	Lat* (°)	Lon* (°)	Mw	RMSE (cm)
					Segment1 (F1)						
Min	1	0	0	0	0	0	0.1				
Max	15	8	5	90	270	180	5				
Optimum	5.06	5.80	1.58	60.3	232.3	107.5	0.67				
								78.634	41.145		
94% HDI	5.00-5.16	4.78-6.90	1.33-1.84	58.4-62.3	228.8-235.7	100.2-114.6	0.57-0.78				
										5.88	4.81
					Segment2 (F2)						
Min	1	0	0	0	0	0	0.1				
Max	15	8	5	90	270	180	5				
Optimum	6.36	1.14	1.22	58.3	2.2	42.8	0.68				
								78.634	41.112		
94% HDI	6.02-6.69	0.36-2.17	0.77-1.59	52.4-64.0	0.0-4.8	35.9-50.0	0.22-1.31				

*lat/lon: start point coordinate of the fault upper edge

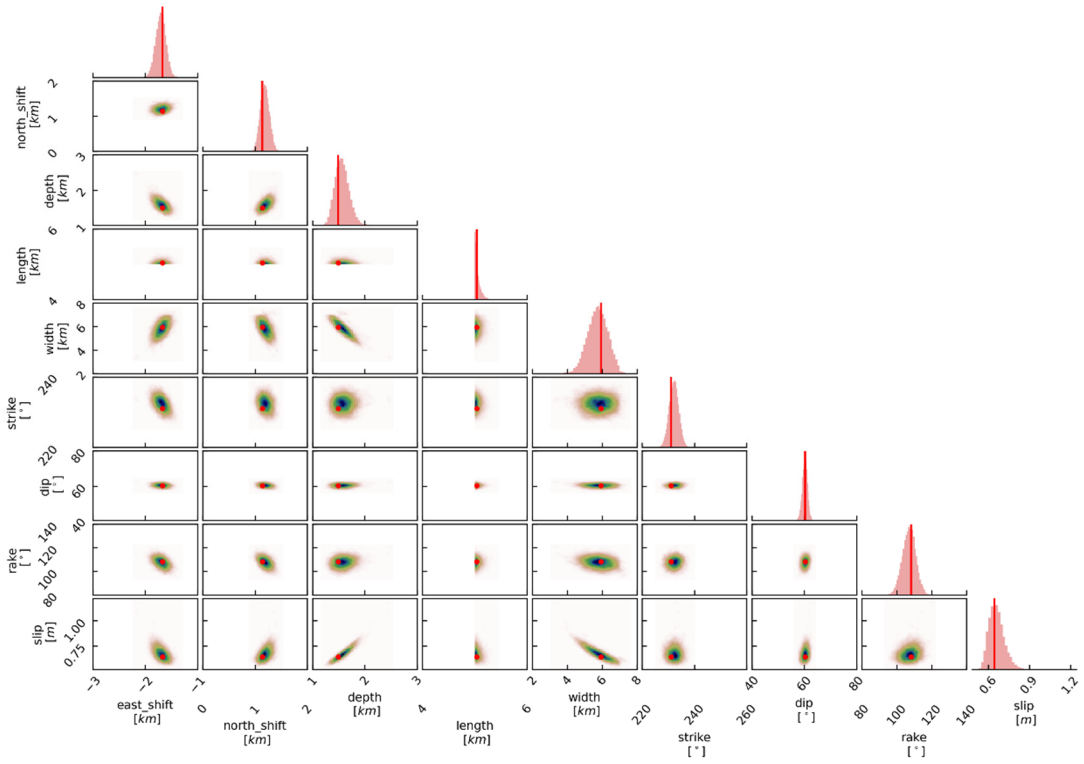

Figure S11. 1D/2D marginal posterior probability densities of the estimated fault parameters for F1 fault.

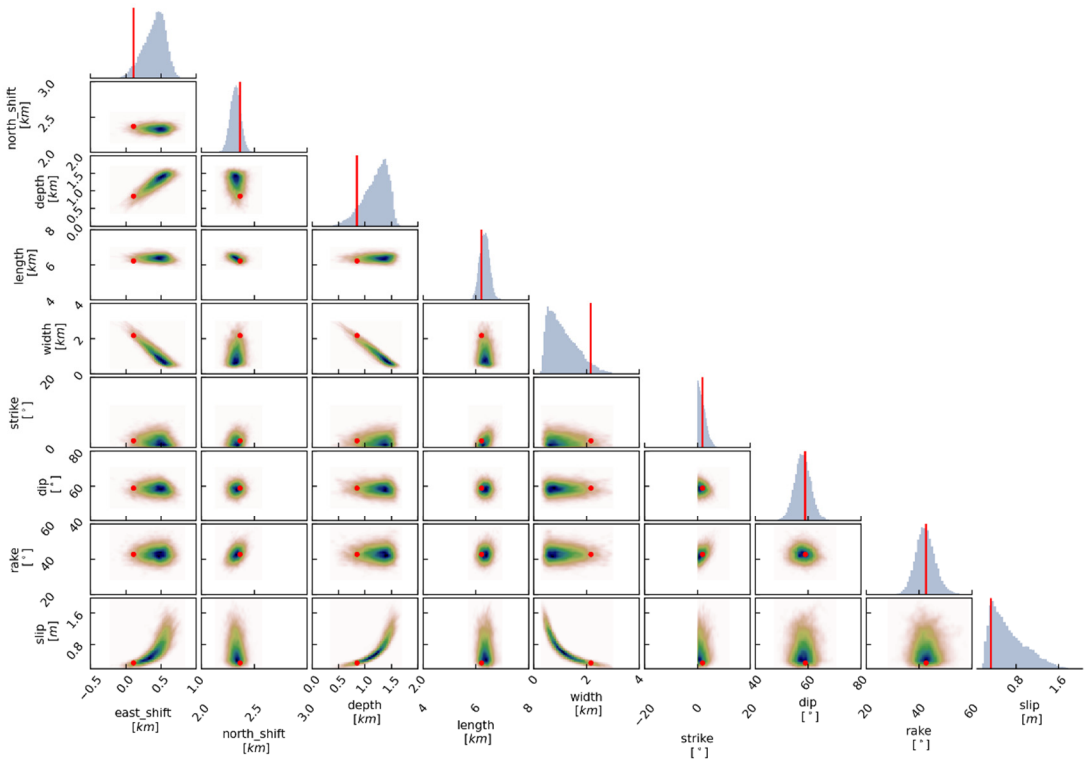

Figure S12. 1D/2D marginal posterior probability densities of the estimated fault parameters for F2 fault.

S3.4 SW-dipping two-fault model

Table S6. Seismogenic fault parameters for the SW-dipping two-fault model.

	Length (km)	Width (km)	Depth (km)	Dip (°)	Strike (°)	Rake (°)	Slip (m)	Lat* (°)	Lon* (°)	Mw	RMSE (cm)
					Segment1						
Min	-*	-	0	-	-	80	0				
Max	-	-	10	-	-	100	5				
Optimum	5	8	0.12	60	61	107	0.38				
								41.14	78.59		
94% HDI	-	-	0.00-0.24	-	-	105-110	0.34-0.43				
										5.98	6.1
					Segment2						
Min	-	-	0	-	-	170	0				
Max	-	-	10	-	-	180	5				
Optimum	4	3.5	4.88	76	191	178	6.50	41.16	78.66		
94% HDI	-	-	4.67-5.01	-	-	175-180	5.77-7.27				

*lat/lon: start point coordinate of the fault upper edge

-*: fixed parameters

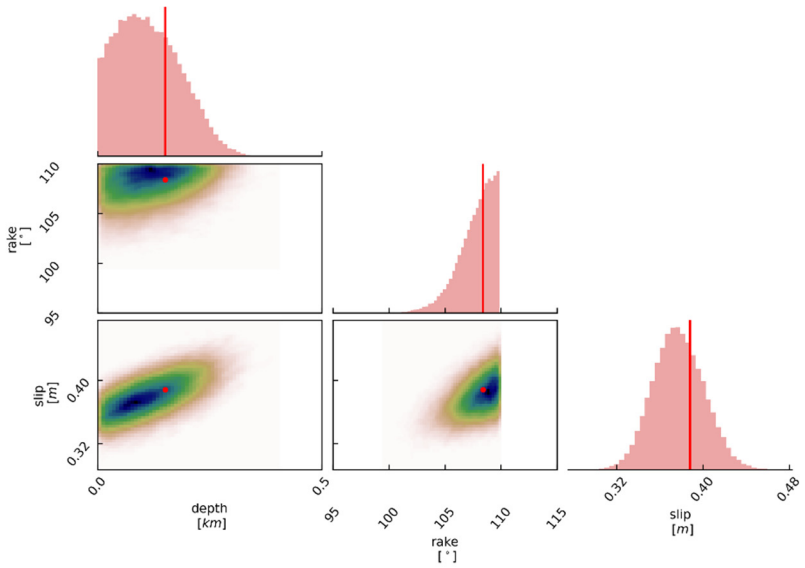

Figure S13. 1D/2D marginal posterior probability densities of the estimated fault parameters for F1 fault.

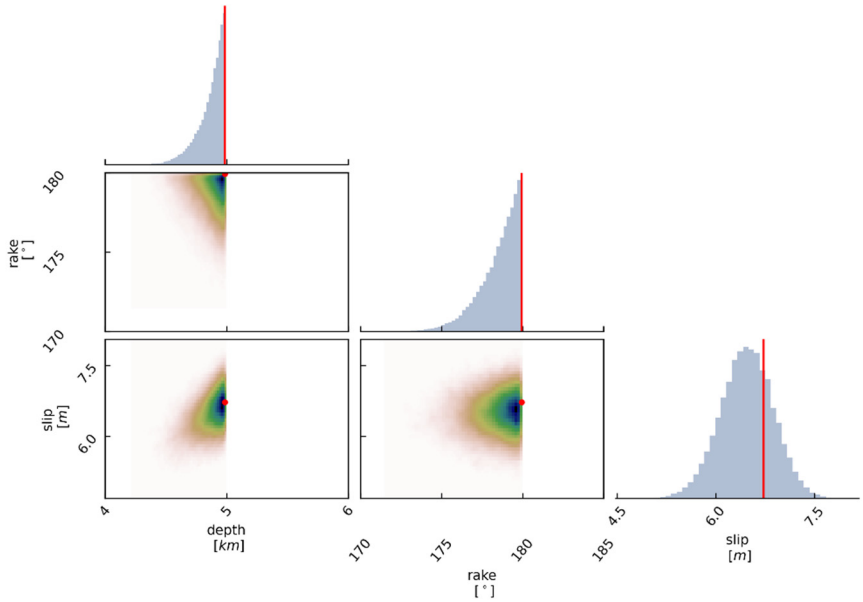

Figure S14. 1D/2D marginal posterior probability densities of the estimated fault parameters for F1 fault.

S4. Viscoelastic relaxation

This section illustrates the modeling approach and modeling results of viscoelastic relaxation process for the 11-month post-seismic deformation.

We used the CRUST1.0 model [37] to obtain the depth of the crust layers. The thickness of the upper crust and lower crust are 30.02 km and 19.28 km, respectively. The depth of the Moho is 49.3 km. The viscosities range for the lower crust (η_{lc}) and upper mantle (η_{um}) is $1 \times 10^{17}\ Pas$ to $1 \times 10^{21}\ Pas$, and the step is $\log_{10}\eta = 1$.

We used the RELAX software [50] to simulate the 11-month post-seismic deformation caused by viscoelastic relaxation. The grid search method was used to obtain the best-fitting viscosities and the RMSE index was used to evaluate the model fitting.

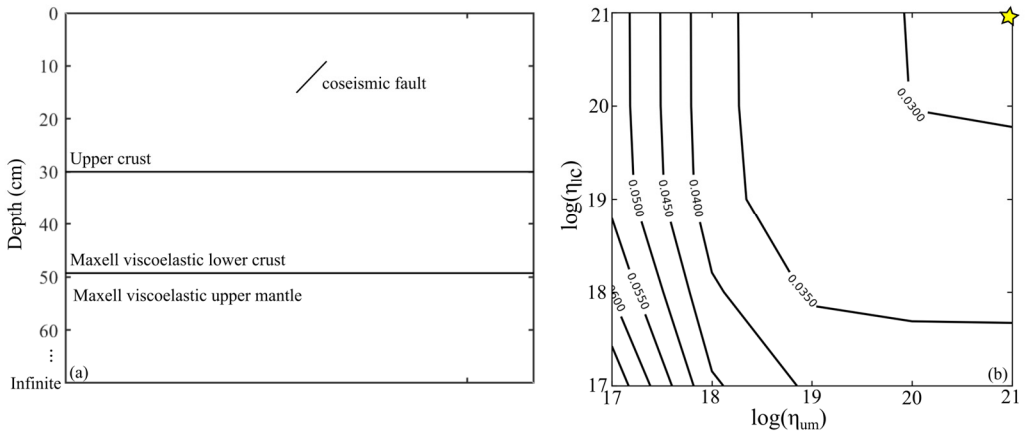

Figure S15. (a) Layer model of the study region. The black solid line represents the coseismic fault. (b) Misfit (RMSE with unit of m) contour map in η_{lc} and η_{um} space. The yellow star indicates the best-fitting model.

Our results showed that the best-fitting parameters of η_{lc} and η_{um} were $1 \times 10^{21} Pas$ and $1 \times 10^{21} Pas$, respectively. The RMSE of the best-fitting model was 2.98 cm, which was much larger than that of the best-fitting afterslip model (0.57 cm). Besides, we also compared the spatial pattern of observation and simulation (Figure S16) and found that there was almost no similarity between them. Therefore, both the quantitative and qualitative comparisons illustrated that afterslip was the primarily process for the 11-month post-seismic deformation.

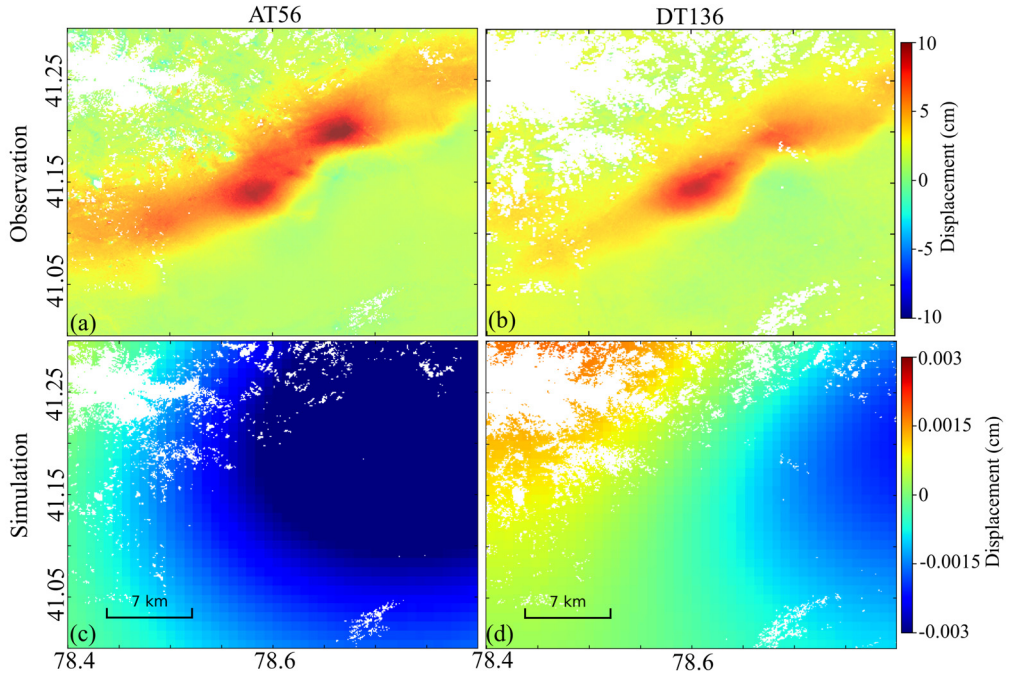

Figure S16. Comparison of spatial pattern between 11-month post-seismic observation and 11-month viscoelastic relaxation best-fitting simulation. (a) and (b) observation for ascending and descending track, respectively. (c) and (d) best-fitting simulation for ascending and descending track, respectively.